Holonomic Quantum Control by Coherent Optical Excitation in Diamond

Brian B. Zhou,[1] Paul C. Jerger,[1] V. O. Shkolnikov,[2] F. Joseph Heremans,[1,3] Guido Burkard,[2] and David D. Awschalom[1,3,*]
[1]Institute for Molecular Engineering, University of Chicago, Chicago, Illinois 60637, USA
[2]Department of Physics, University of Konstanz, D-78457 Konstanz, Germany
[3]Materials Science Division, Argonne National Laboratory, Argonne, Illinois 60439, USA
(Received 1 May 2017; published 2 October 2017)

Although geometric phases in quantum evolution are historically overlooked, their active control now stimulates strategies for constructing robust quantum technologies. Here, we demonstrate arbitrary single-qubit holonomic gates from a single cycle of nonadiabatic evolution, eliminating the need to concatenate two separate cycles. Our method varies the amplitude, phase, and detuning of a two-tone optical field to control the non-Abelian geometric phase acquired by a nitrogen-vacancy center in diamond over a coherent excitation cycle. We demonstrate the enhanced robustness of detuned gates to excited-state decoherence and provide insights for optimizing fast holonomic control in dissipative quantum systems.

DOI: 10.1103/PhysRevLett.119.140503

Besides its central role in the understanding of contemporary physics [1,2], the quantum geometric phase is gaining recognition as a powerful resource for practical applications using quantum systems [3–5]. The manipulation of nanoscale systems has progressed rapidly towards realizing quantum-enhanced information processing and sensing, but has also revealed the necessity for new methods to combat noise and decoherence [6–8]. Because of their intrinsic tolerance to local fluctuations [9,10], geometric phases offer an attractive route for implementing high-fidelity quantum logic. This approach, termed holonomic quantum computation (HQC) [3,11–15], employs the cyclic evolution of quantum states and derives its resilience from the global geometric structure of the evolution in Hilbert space. Arising both for adiabatic [16] and nonadiabatic [17] cycles, geometric phases can be either Abelian (phase shifts) or non-Abelian (matrix transformations) [18] by acting on a single state or a subspace of states, respectively.

Recently, non-Abelian, nonadiabatic holonomic gates using three-level dynamics [19] were proposed to match the computational universality of earlier adiabatic schemes [3,11–13], but also eliminate the restriction of slow evolution. By reducing the run time of holonomic gates, and thus their exposure to decoherence, this advance enabled experimental demonstration of HQC in superconducting qubits [20], nuclear spin ensembles in liquid [21], and nitrogen-vacancy (NV) centers in diamond [22,23]. However, these initial demonstrations were limited to fixed rotation angles about arbitrary axes, and thus required two nonadiabatic loops of evolution, from two iterations of experimental control, to execute an arbitrary gate [20–23]. Alternatively, variable angle rotations from a single nonadiabatic loop can be achieved using Abelian geometric phases [14,24] or hyperbolic secant pulses [25–27], but these approaches are complicated by a concomitant dynamic phase. To address these shortcomings, non-Abelian, nonadiabatic single-loop schemes [28,29] were designed to allow purely geometric, arbitrary angle rotations about arbitrary axes with a single experimental iteration.

In this Letter, we realize single-loop, single-qubit holonomic gates by implementing the proposal of Ref. [29] in a Λ system formed by optical transitions in the NV center. Our approach controls the common detuning and the relative amplitude and phase of a two-tone optical field that drives two nondegenerate transitions of the Λ system. By working with detuned optical driving to an excited state rather than with resonant microwaves within the ground state [22,23], we not only provide single-cycle operation and enhanced spatial resolution, but also characterize how decoherence affects gate operation. We perform quantum process tomography on an overcomplete set of resonant and off-resonant gates to demonstrate superior fidelities for off-resonant gates due to decreased excitation to the lossy intermediate state. This reveals that the detuned, single-cycle gates can offer an advantage beyond simply eliminating one pulse in the equivalent gate by two resonant pulses.

Methods.—We utilize a naturally occurring, single NV center in bulk diamond cooled to 5 K. Below 20 K, optical transitions from the NV spin-triplet ground state to its spin-triplet excited state resolve narrow lines corresponding to the fine structure of the orbital-doublet excited state [Figs. 1(a) and 1(b)] [30]. Spin-spin and spin-orbit interactions lead to optical selection rules that enable spin-photon entanglement, as well as cycling transitions and Λ energy structures, establishing the NV center as a leading platform for quantum optics and communication demonstrations [10,31–34]. Here, we connect the $|m_S = -1\rangle$ and $|m_S = +1\rangle$ ground states to the highest-lying excited state $|A_2\rangle$ via a single tunable laser that is electro-optically modulated to generate frequency sidebands and nanosecond pulses [34]. We split the $|\pm 1\rangle$ states by 1.461 GHz (261 G magnetic field) and match the sideband separation to this splitting to simultaneously address both transitions, as identified in red in the photoluminescence excitation scan [Fig. 1(b)]. Because of the low

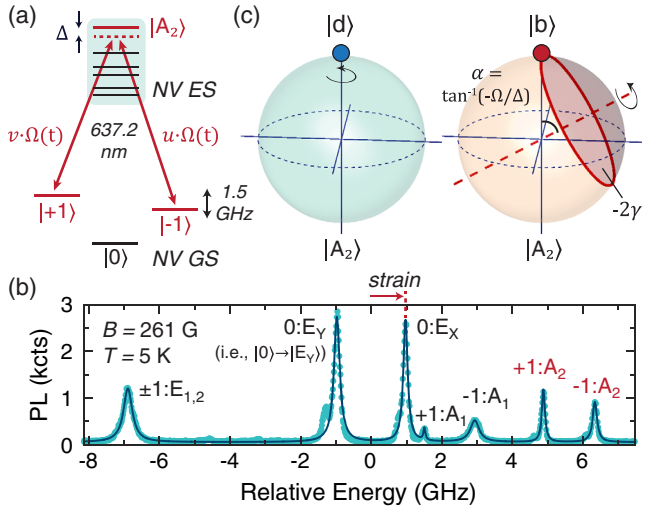

FIG. 1. Experimental system and holonomic concept. (a) Optical NV Λ system. The $|\pm 1\rangle$ spin states of the NV triplet ground state (GS) are linked to $|A_2\rangle$ within the spin-orbit excited-state (ES) manifold by a two-tone optical field with one-photon detuning Δ and strength $\Omega(t)$. (b) Photoluminescence excitation spectrum taken by scanning a single laser frequency across the GS to ES transitions while two microwave tones mix the population among the three GS levels. (c) Geometric interpretation of the holonomic gates. The dark state $|d\rangle$ undergoes trivial dynamics, while the bright state $|b\rangle$ undergoes precession around a tilted axis with angle α on the $|b\rangle/|A_2\rangle$ Bloch sphere. After one nonadiabatic cycle, $|b\rangle$ acquires a geometric phase γ proportional to the enclosed solid angle.

strain of 0.97 GHz, the three connected levels form a nearly ideal Λ system [31].

In the rotating frame, our system is described by the Hamiltonian

$$H(t) = \frac{\hbar\Omega(t)}{2}(u|A_2\rangle\langle -1| + v|A_2\rangle\langle +1| + \text{H.c.}) + \Delta|A_2\rangle\langle A_2|, \tag{1}$$

where $\Omega(t)$ describes the pulse envelope common to both tones and Δ is the one-photon detuning [Fig. 1(a)]. The individual transition amplitudes are scaled by the complex constants $u = \sin(\frac{\theta}{2})$ and $v = -\cos(\frac{\theta}{2})e^{-i\phi}$, which are controlled by tuning the relative strength and phase between the carrier and sideband frequencies. Because of the condition of two-photon resonance, this Hamiltonian admits a dark state $|d\rangle = \cos(\frac{\theta}{2})|-1\rangle + \sin(\frac{\theta}{2})e^{i\phi}|+1\rangle$ that is decoupled from the dynamics, and a bright state $|b\rangle = \sin(\frac{\theta}{2})|-1\rangle - \cos(\frac{\theta}{2})e^{i\phi}|+1\rangle$, which undergoes excitation to $|A_2\rangle$. When $\Omega(t)$ is a square pulse [i.e., $\Omega(t) = \Omega$ for $0 \le t \le \tau$], $H(t)$ is time independent during the dynamics. Thus, the expected value of the energy is conserved, remaining zero during the evolution for any initial state starting in the subspace spanned by $|\pm 1\rangle$ and ensuring the absence of a dynamic phase. However, for the pulse duration $\tau = 2\pi/\sqrt{\Omega^2 + \Delta^2} \equiv T_{2\pi}$, this computational subspace undergoes cyclic, nonadiabatic evolution and transforms via the purely geometric evolution operator $U(\theta,\phi,\Delta/\Omega) = |d\rangle\langle d| + e^{i\gamma}|b\rangle\langle b| = e^{i\gamma/2}e^{-i(\gamma/2)\mathbf{n}\cdot\boldsymbol{\sigma}}$ [29], where $\mathbf{n} = (\sin\theta\cos\phi, \sin\theta\sin\phi, \cos\theta)$, $\boldsymbol{\sigma}$ are the Pauli matrices, and

$$\gamma = \pi(1 - \Delta/\sqrt{\Omega^2 + \Delta^2}). \tag{2}$$

Up to a global phase, $U(\theta,\phi,\Delta/\Omega)$ represents a rotation by angle γ about the axis $\mathbf{n}$ in the Bloch sphere with poles $|z\rangle = |-1\rangle$ and $|-z\rangle = |+1\rangle$, thus realizing arbitrary, noncommuting gates in a single cycle. Geometric insight is obtained by considering γ to be the Abelian geometric phase acquired by the bright state $|b\rangle$ and equal to $-A/2$, where A is the solid angle traced by $|b(t)\rangle$'s nonadiabatic precession [Fig. 1(c)] [22,29].

Recently, Ref. [35] presented an investigation of the described scheme using the $|A_2\rangle$ Λ system at a zero magnetic field. There, a single-tone optical field addresses both degenerate transitions, while its polarization determines the bright state superposition of $|\pm 1\rangle$ that couples to $|A_2\rangle$ owing to special polarization-dependent selection rules. Rather than using this elegant but atypical correspondence

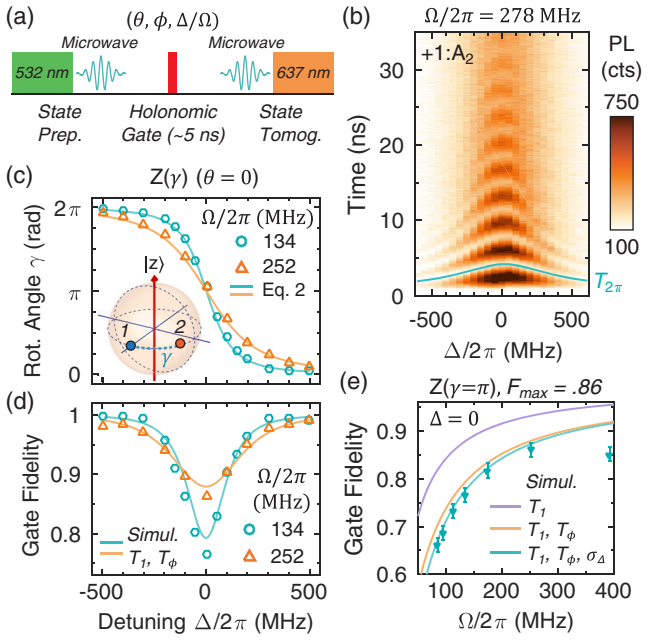

FIG. 2. Phase shift gates $Z(\gamma)$. (a) Experimental sequence consisting of state preparation, optical excitation with control parameters $(\theta, \phi, \Delta/\Omega)$, and state tomography. (b) Time-resolved photoluminescence, proportional to the $|A_2\rangle$ population, as a function of detuning Δ, showing oscillations between $|b\rangle = |+1\rangle$ and $|A_2\rangle$ $(\theta = 0)$. (c) Measured phase shifts γ, averaged over $|x\rangle$ and $|y\rangle$ input states, as a function of Δ for $Z(\gamma)$ at two different optical powers. The solid lines delineate the prediction according to Eq. (2). (d) Gate fidelities via process tomography of the same $Z(\gamma)$ gates. The solid lines are simulated fidelities incorporating an excited-state lifetime T_1 and dephasing T_ϕ. (e) Dependence of the fidelity of the resonant gate $Z(\gamma = \pi)$ on Ω. The purple, orange, and teal lines represent the simulated fidelities by sequentially adding the effects of T_1, T_ϕ, and the spectral hopping σ_Δ.

between polarization and qubit states, our application instead employs a two-tone field that is generalizable to widespread nondegenerate three-level systems [20,36–41]. Additionally, we perform process tomography on a universal set of single-qubit gates, including Hadamard and off-resonant gates, and identify strategies to minimize decoherence during holonomic control.

Our experiments begin by initializing the standard states $|x\rangle$, $|y\rangle$, $|\pm z\rangle$ on the $|\pm 1\rangle$ Bloch sphere [Fig. 2(a)] [42]. Subsequently, a short laser pulse with parameters $(\theta, \phi, \Delta/\Omega)$ implements the appropriate holonomic gate, and the resulting state is characterized by tomography along the same basis set. To determine the optical coupling Ω (in units of Rabi frequency) and the time $T_{2\pi}$ of a single excitation cycle, we measure the time-resolved photoluminescence, due to spontaneous emission from $|A_2\rangle$, during a continuous square pulse with the same $(\theta, \phi, \Delta/\Omega)$. Figure 2(b) shows typical coherent oscillations of the population between the bright state $|b\rangle = |+1\rangle$ and $|A_2\rangle$ as a function of detuning for a drive field on the $|+1\rangle$ to $|A_2\rangle$ transition ($\theta = 0$).

Results.—We start by characterizing arbitrary rotations about the z axis via the gate set $Z(\gamma)$ with $\theta = 0$. This family includes the widely used phase shift operations Pauli Z, S, and T, corresponding to $\gamma = \pi, \pi/2$, and $\pi/4$, respectively. In Fig. 2(c), we measure the phase shift γ acquired as a function of detuning Δ for the $|x\rangle$ and $|y\rangle$ input states. We extract γ from the difference between the phases φ of the input and output states, where $\varphi = \tan^{-1}(Y_p/X_p)$ using the Bloch vector projections X_p (Y_p) along the x (y) axis. The data for two different Ω show good agreement with Eq. (2), delineated by the solid lines.

Using quantum process tomography, we demonstrate that the off-resonant $Z(\gamma \neq \pi)$ gates obtain higher fidelities than the resonant Pauli Z gate [Fig. 2(d)]. Since the dominant loss mechanisms stem from $|A_2\rangle$, detuned driving reduces this detrimental exposure by decreasing both the maximal excitation and gate operation time. The solid lines in Fig. 2(d) represent the expected fidelities from a master equation simulation [42] that uses an excited-state lifetime ($T_1 = 11.1$ ns) and dephasing ($T_\phi = 18$ ns) as previously measured for this NV center [34]. Furthermore, we demonstrate that the fidelity of the resonant Pauli Z gate increases as the run time $T_{2\pi} \propto \Omega^{-1}$ decreases [Fig. 2(e)] [45]. We separate the theoretical contributions to decoherence due to the lifetime T_1 and dephasing T_ϕ by incorporating their effects sequentially. The remaining discrepancy with the data, particularly at low optical powers, is largely reconciled by introducing spectral hopping of the excited state's energy, modeled by detuning errors with a Gaussian standard deviation $\sigma_\Delta = 2\pi \times 15$ MHz. The experimental fidelities saturate at $F = 0.86(2)$ for $\Omega/2\pi > 252$ MHz due to cross-talk with nearby levels [Fig. 1(b)] and laser leakage before and after the pulse caused by a finite extinction ratio [42].

We proceed to examine resonant holonomic π rotations about arbitrary axes in Fig. 3. Before focusing on process tomography of the Pauli X, Pauli Y, and Hadamard gates (denoted X, Y, H, respectively [42]), we verify full control over the (θ, ϕ) degrees of freedom and illuminate how the relationship between the gate's input state and the dark or bright state axis affects decoherence. In Fig. 3(a), we initialize $|z\rangle$ and apply gates with variable θ, holding $\phi = 0$. As schematically illustrated, this holonomic

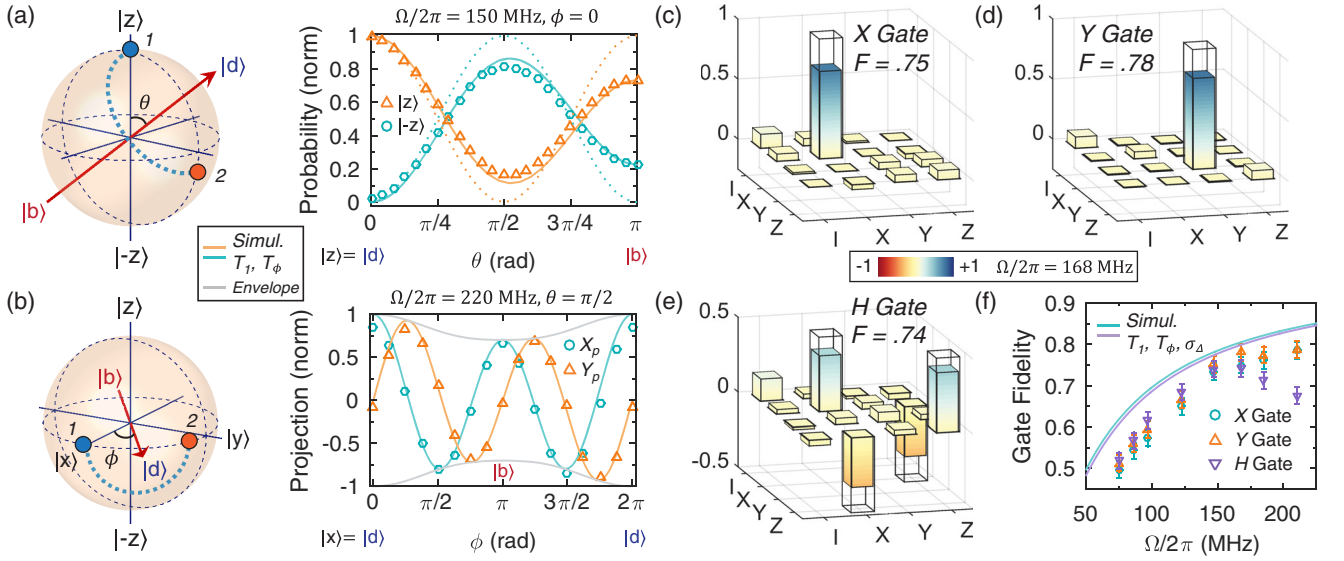

FIG. 3. Resonant holonomic gates. (a) Gates with variable θ after initializing $|z\rangle$. The probabilities of the final states to be measured in $|z\rangle$ and $|-z\rangle$ are plotted. (b) Gates with variable ϕ after initializing $|x\rangle$. The Bloch vector projections of the final states along the x and y axes are plotted. For both (a) and (b), solid lines indicate simulated behaviors with T_1 and T_ϕ decoherence; the dashed lines in (a) indicate decoherence-free behavior. Decoherence is minimized when the initialized state aligns with the gate's dark state $|d\rangle$. (c)–(e) Process matrices for X, Y, and H at $\Omega/2\pi = 168$ MHz. (f) Dependence of X, Y, H process fidelities on Ω. The solid lines are simulated fidelities incorporating all excited-state decoherence effects. X and Y are identical in the simulation.

transformation induces effective Rabi oscillations between $|z\rangle$ and $|-z\rangle$ as θ is increased. Notably, the discrepancy between the realized population transfer (data points) and the decoherence-free transfer (dashed lines) varies as a function of θ, being smallest (largest) at $\theta = 0$ ($\theta = \pi$) when the initialized state $|z\rangle$ is the dark (bright) state of the gate [Fig. 3(a)]. Correspondingly, we initialize $|x\rangle$ and apply gates with variable ϕ, holding $\theta = \pi/2$ [Fig. 3(b)]. In this case, we display X_p and Y_p of the final state, showing it to rotate around the equator twice as ϕ rotates once, as expected. The visibility of the final state (gray envelope) is maximal (minimal) when $|x\rangle$ is aligned with the gate's dark (bright) state. Since the on-resonant gates (π rotations) are invariant under interchange of $|d\rangle$ and $|b\rangle$, there exist two equivalent choices $\{\theta, \theta + \pi\}$ for each gate in the absence of dissipation. However, for implementations where the intermediate state dominates loss, our observations demonstrate that when the input state $|\psi_i\rangle$ is known (e.g., in state preparation), the more effective holonomic gate minimizes $|\langle\psi_i|b\rangle|^2$.

We achieve process fidelities for X, Y, and H of 0.75(2), 0.78(2), and 0.74(2), respectively, at $\Omega/2\pi = 168$ MHz [Figs. 3(c)–3(e)]. The fidelities of these gates display a similar scaling versus Ω as the Z gate. However, when comparing with the simulated fidelities (solid lines) using the same excited-state T_1, T_ϕ, and σ_Δ, the data for X, Y, and H realize lower fidelities than expected by our model [Fig. 3(f)]. This is explained by the presence of additional experimental nonidealities from turning on two drive frequencies, such as enhanced crosstalk, relative phase errors, and extraneous higher-harmonic sidebands. We improve the fidelity of X and Y to 0.79(2) at $\Omega/2\pi = 210$ MHz, but H decreases in fidelity. This effect may stem from the greater susceptibility of H to systematic errors.

Finally, we demonstrate tunable rotations around the x and y axes by varying the detuning of the optical pulse. Initializing $|z\rangle$, we verify that these gates rotate the population from $|z\rangle$ to $|-z\rangle$ and back as the laser frequency is varied across one-photon resonance [Fig. 4(a), $\theta = \pi/2$]. Focusing on $\Delta/\Omega = \pm 1/\sqrt{3}$ for $\Omega/2\pi = 152$ MHz, we realize process fidelities for the $X(\pi/2)$ (i.e., $\sqrt{\text{NOT}}$ gate), $X(-\pi/2)$, $Y(\pi/2)$, and $Y(-\pi/2)$ gates of 0.83(2), 0.80(2), 0.82(2), and 0.80(2), respectively, where the sign of the rotation is controlled by the sign of Δ [Figs. 4(b)–4(d)] [42]. Because of decreased excitation, these gate fidelities exceed those of the resonant gates at the same optical power (~ 0.74 at $\Omega/2\pi = 150$ MHz). In the resonant scheme for nonadiabatic HQC [19], arbitrary angle rotations required two π rotations around different axes: for example, $Y(\pi/2) = XH$. Our data demonstrate that in applications involving dissipative intermediate states, the single-loop scheme significantly outperforms the equivalent composite gate, which would achieve here an estimated fidelity of 0.55 ($\approx 0.74^2$), and moreover exceeds the fidelity of a single resonant gate. In comparison, if the single-loop gates are implemented by microwave driving within the ground state [22,23], the

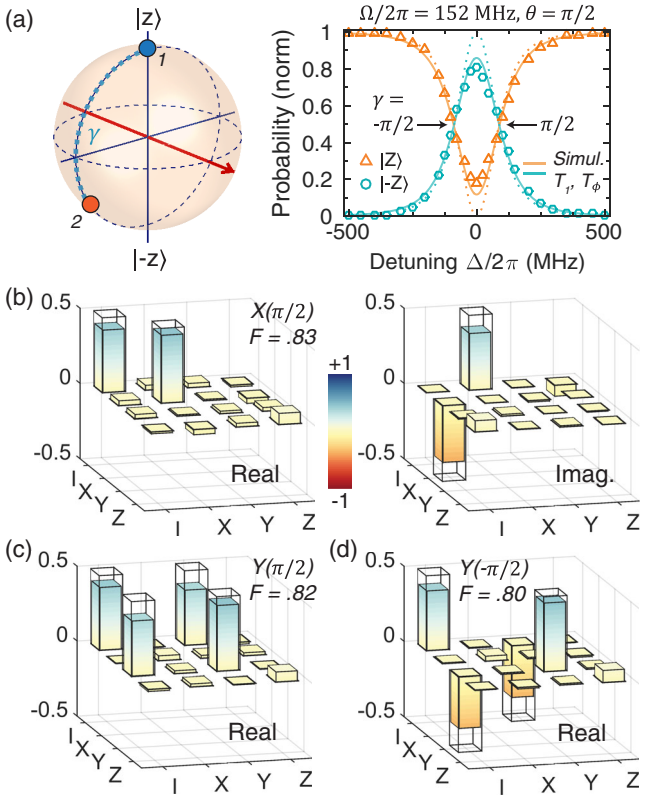

FIG. 4. Variable rotations around the x and y axes. (a) After initializing $|z\rangle$, a holonomic gate with variable detuning Δ and a fixed rotation axis along $|x\rangle$ is applied. The data show Rabi oscillations between $|z\rangle$ and $|-z\rangle$ as Δ is swept across resonance, tuning the rotation angle γ. The solid lines are simulations with T_1 and T_ϕ decoherence; the dashed lines are decoherence-free behaviors. (b)–(d) Process matrices for the $X(\pi/2)$ and $Y(\pm\pi/2)$ gates at $\Omega/2\pi = 152$ MHz and $\Delta/2\pi = \pm 88$ MHz.

intermediate level $|m_S = 0\rangle$ would decohere at a rate (limited by ground-state dephasing $T_2^* \sim 10$ μs) comparable to the computational states $|\pm 1\rangle$. This extended coherence enables higher fidelities, but decreased occupation of $|0\rangle$ by off-resonant driving would not be an advantage beyond its reduction in the number of gates applied.

Discussion.—The optical gate fidelities are limited by excited-state occupation and crosstalk between the driving fields. Improving the rise time and extinction of our optical pulses would enable faster transit through the excited state without side effects and also reduce errors due to the dynamic phase for the detuned gates, which are fully geometric only for perfect square pulses [29]. Although for $\Omega/2\pi = 152$ MHz, the current rise or fall times ($\sim$1.2 ns) contribute negligible errors to $X(\pi/2)$, we estimate that dynamic errors would begin to limit the fidelity for $\Omega/2\pi > 600$ MHz [42]. Crosstalk between the Λ transitions can be improved by using orthogonal polarizations for the two driving frequencies, rather than the same linear polarization, to exploit the polarization selectivity of the transitions. In Ref. [35], faster gate speeds and

reduced crosstalk in the single-tone implementation enabled fidelities of ∼0.90 for the resonant Pauli gates, while calculations are required to compensate the driving polarization for each specific NV strain and orientation.

Our experiments establish universal single-qubit holonomic control of solid-state spins with optical spatial resolution and single-cycle operation. A path toward two-qubit gates and universal computation is envisioned by leveraging strong coupling to nearby nuclear spins [46] or cavity-mediated interactions to other NV centers [47,48]. Fundamentally, our holonomic operations are efficient in both time and number of control parameters for the arbitrary manipulation of qubit levels that are not directly coupled. Thus, they are relevant to hybrid systems where disparate quantum systems are indirectly linked via an intermediary. Holonomic state transfer may be more efficient than sequential, multipulse operations through the dissipative intermediate system [49]. Additionally, our methods offer an alternative when far-detuned stimulated Raman transitions ($\Delta \gg \Omega$), which effect much slower rotations, are impractical due to the interplay between decoherence rates and level separations [50–52]. The strategies demonstrated here for optimizing fast holonomic control enrich the quantum control toolbox to adapt to a growing diversity of useful quantum systems.

We thank C. G. Yale and A. Baksic for valuable discussions. This work was supported by the Air Force Office of Scientific Research MURI No. FA9550-15-1-0029 and No. FA9550-14-1-0231, and National Science Foundation Grant No. DMR-1306300. F. J. H. and D. D. A. contributed to the experimental design, analysis of data, and preparation of the manuscript and were supported by the U.S. Department of Energy, Office of Science, Office of Basic Energy Sciences, Materials Sciences and Engineering Division. Work at the University of Konstanz was supported by the German Research Foundation (SFB 767).

Note added.—Recently, we became aware of two complementary works [35,53].

*awsch@uchicago.edu

[1] F. Wilczek and A. Shapere, *Geometric Phases in Physics* (World Scientific, Singapore, 1989).
[2] D. Xiao, M. C. Chang, and Q. Niu, Rev. Mod. Phys. **82**, 1959 (2010).
[3] P. Zanardi and M. Rasetti, Phys. Lett. A **264**, 94 (1999).
[4] M. P. Ledbetter, K. Jensen, R. Fischer, A. Jarmola, and D. Budker, Phys. Rev. A **86**, 052116 (2012).
[5] E. Martín-Martínez, A. Dragan, R. B. Mann, and I. Fuentes, New J. Phys. **15**, 053036 (2013).
[6] D. A. Lidar, I. L. Chuang, and K. B. Whaley, Phys. Rev. Lett. **81**, 2594 (1998).
[7] E. Knill, R. Laflamme, and L. Viola, Phys. Rev. Lett. **84**, 2525 (2000).
[8] C. Nayak, S. H. Simon, A. Stern, M. Freedman, and S. Das Sarma, Rev. Mod. Phys. **80**, 1083 (2008).
[9] S. Berger, M. Pechal, A. A. Abdumalikov, C. Eichler, L. Steffen, A. Fedorov, A. Wallraff, and S. Filipp, Phys. Rev. A **87**, 060303 (2013).
[10] C. G. Yale, F. J. Heremans, B. B. Zhou, A. Auer, G. Burkard, and D. D. Awschalom, Nat. Photonics **10**, 184 (2016).
[11] A. Ekert, M. Ericsson, P. Hayden, H. Inamori, J. A. Jones, D. K. L. Oi, and V. Vedral, J. Mod. Opt. **47**, 2501 (2000).
[12] L. M. Duan, J. I. Cirac, and P. Zoller, Science **292**, 1695 (2001).
[13] L. Faoro, J. Siewert, and R. Fazio, Phys. Rev. Lett. **90**, 028301 (2003).
[14] S.-L. Zhu and Z. D. Wang, Phys. Rev. Lett. **89**, 097902 (2002).
[15] E. Sjöqvist, V. Azimi Mousolou, and C. M. Canali, Quantum Inf. Process. **15**, 3995 (2016).
[16] M. V. Berry, Proc. R. Soc. A **392**, 45 (1984).
[17] Y. Aharonov and J. Anandan, Phys. Rev. Lett. **58**, 1593 (1987).
[18] F. Wilczek and A. Zee, Phys. Rev. Lett. **52**, 2111 (1984).
[19] E. Sjöqvist, D. M. Tong, L. Mauritz Andersson, B. Hessmo, M. Johansson, and K. Singh, New J. Phys. **14**, 103035 (2012).
[20] A. A. Abdumalikov, J. M. Fink, K. Juliusson, M. Pechal, S. Berger, A. Wallraff, and S. Filipp, Nature (London) **496**, 482 (2013).
[21] G. Feng, G. Xu, and G. Long, Phys. Rev. Lett. **110**, 190501 (2013).
[22] C. Zu, W.-B. Wang, L. He, W.-G. Zhang, C.-Y. Dai, F. Wang, and L.-M. Duan, Nature (London) **514**, 72 (2014).
[23] S. Arroyo-Camejo, A. Lazariev, S. W. Hell, and G. Balasubramanian, Nat. Commun. **5**, 4870 (2014).
[24] L. Wang, T. Tu, B. Gong, C. Zhou, and G.-C. Guo, Sci. Rep. **6**, 19048 (2016).
[25] S. E. Economou and T. L. Reinecke, Phys. Rev. Lett. **99**, 217401 (2007).
[26] P. Pei, F.-Y. Zhang, C. Li, and H.-S. Song, J. Phys. B: At. Mol. Opt. Phys. **43**, 125504 (2010).
[27] Y. Kodriano, I. Schwartz, E. Poem, Y. Benny, R. Presman, T. A. Truong, P. M. Petroff, and D. Gershoni, Phys. Rev. B **85**, 241304 (2012).
[28] G. F. Xu, C. L. Liu, P. Z. Zhao, and D. M. Tong, Phys. Rev. A **92**, 052302 (2015).
[29] E. Sjöqvist, Phys. Lett. A **380**, 65 (2016).
[30] A. Batalov, V. Jacques, F. Kaiser, P. Siyushev, P. Neumann, L. J. Rogers, R. L. McMurtrie, N. B. Manson, F. Jelezko, and J. Wrachtrup, Phys. Rev. Lett. **102**, 195506 (2009).
[31] E. Togan, Y. Chu, A. S. Trifonov, L. Jiang, J. Maze, L. Childress, M. V. G. Dutt, A. S. Sørensen, P. R. Hemmer, A. S. Zibrov, and M. D. Lukin, Nature (London) **466**, 730 (2010).
[32] B. Hensen *et al.*, Nature (London) **526**, 682 (2015).
[33] S. Yang, Y. Wang, D. D. B. Rao, T. Hien Tran, A. S. Momenzadeh, M. Markham, D. J. Twitchen, P. Wang, W. Yang, R. Stöhr, P. Neumann, H. Kosaka, and J. Wrachtrup, Nat. Photonics **10**, 507 (2016).
[34] B. B. Zhou, A. Baksic, H. Ribeiro, C. G. Yale, F. J. Heremans, P. C. Jerger, A. Auer, G. Burkard, A. A. Clerk, and D. D. Awschalom, Nat. Phys. **13**, 330 (2017).
[35] Y. Sekiguchi, N. Niikura, R. Kuroiwa, H. Kano, and H. Kosaka, Nat. Photonics **11**, 309 (2017).

[36] M. Kasevich and S. Chu, Phys. Rev. Lett. **69**, 1741 (1992).
[37] L. V. Hau, S. E. Harris, Z. Dutton, and C. H. Behroozi, Nature (London) **397**, 594 (1999).
[38] B. Pingault, J. N. Becker, C. H. H. Schulte, C. Arend, C. Hepp, T. Godde, A. I. Tartakovskii, M. Markham, C. Becher, and M. Atatüre, Phys. Rev. Lett. **113**, 263601 (2014).
[39] L. J. Rogers, K. D. Jahnke, M. H. Metsch, A. Sipahigil, J. M. Binder, T. Teraji, H. Sumiya, J. Isoya, M. D. Lukin, P. Hemmer, and F. Jelezko, Phys. Rev. Lett. **113**, 263602 (2014).
[40] A. H. Safavi-Naeini, T. P. Mayer Alegre, J. Chan, M. Eichenfield, M. Winger, Q. Lin, J. T. Hill, D. E. Chang, and O. Painter, Nature (London) **472**, 69 (2011).
[41] C. Dong, V. Fiore, M. Kuzyk, and H. Wang, Science **338**, 1609 (2012).
[42] See Supplemental Material at http://link.aps.org/supplemental/10.1103/PhysRevLett.119.140503, which includes Refs. [43] and [44], for additional details on the experiment, data analysis, and simulations.
[43] J. B. Altepeter, D. F. V. James, and P. G. Kwiat, in *Quantum State Estimation*, edited by M. Paris and J. Řeháček, Lecture Notes in Physics, Vol. 649 (Springer, Berlin, 2004), p. 113.
[44] M. Howard, J. Twamley, C. Wittmann, T. Gaebe, F. Jelezko, and J. Wrachtrup, New J. Phys. **8**, 33 (2006).
[45] M. Johansson, E. Sjöqvist, L. M. Andersson, M. Ericsson, B. Hessmo, K. Singh, and D. M. Tong, Phys. Rev. A **86**, 062322 (2012).
[46] F. Jelezko, T. Gaebel, I. Popa, M. Domhan, A. Gruber, and J. Wrachtrup, Phys. Rev. Lett. **93**, 130501 (2004).
[47] G. Burkard, V. O. Shkolnikov, and D. D. Awschalom, Phys. Rev. B **95**, 205420 (2017).
[48] J. Zhou, B.-J. Liu, Z.-P. Hong, and Z.-Y. Xue, arXiv:1705.08852.
[49] Y. D. Wang and A. A. Clerk, New J. Phys. **14**, 105010 (2012).
[50] C. G. Yale, B. B. Buckley, D. J. Christle, G. Burkard, F. J. Heremans, L. C. Bassett, and D. D. Awschalom, Proc. Natl. Acad. Sci. U.S.A. **110**, 7595 (2013).
[51] D. A. Golter and H. Wang, Phys. Rev. Lett. **112**, 116403 (2014).
[52] L. Childress, Science **345**, 1247 (2014).
[53] H. Li, Y. Liu, and G. Long, Sci. China Phys. Mech. Astron. **60**, 080311 (2017).